The Astrophysical Journal, 676:509–517, 2008 March 20

DEBRIS DISKS AROUND NEARBY STARS WITH CIRCUMSTELLAR GAS

Aki Roberge[1]
Exoplanets and Stellar Astrophysics Laboratory, NASA Goddard Space Flight Center, Code 667,
Greenbelt, MD 20771; Aki.Roberge@nasa.gov

and

Alycia J. Weinberger
Department of Terrestrial Magnetism, Carnegie Institution of Washington, 5241 Broad Branch Road NW,
Washington, DC 20015; aweinberger@ciw.edu
Received 2007 August 24; accepted 2007 November 27

ABSTRACT

We conducted a survey for infrared excess emission from 16 nearby main-sequence shell stars using the Multiband Imaging Photometer for *Spitzer* (MIPS) on the *Spitzer Space Telescope*. Shell stars are early-type stars with narrow absorption lines in their spectra that appear to arise from circumstellar (CS) gas. Four of the 16 stars in our survey showed excess emission at 24 and 70 μm characteristic of cool CS dust and are likely to be edge-on debris disks. Including previously known disks, it appears that the fraction of protoplanetary and debris disks among the main-sequence shell stars is at least 48% $\pm$ 14%. While dust in debris disks has been extensively studied, relatively little is known about their gas content. In the case of β Pictoris, extensive observations of gaseous species have provided insights into the dynamics of the CS material and surprises about the composition of the CS gas coming from young planetesimals. To understand the coevolution of gas and dust through the terrestrial planet formation phase, we need to study the gas in additional debris disks. The new debris disk candidates from this *Spitzer* survey double the number of systems in which the gas can be observed right now with sensitive line-of-sight absorption spectroscopy.

Subject headings: circumstellar matter — infrared: stars — planetary systems: formation — stars: early-type

1. INTRODUCTION

Protoplanetary disks may be classified by their relative abundance of primordial gas and dust left over from star formation. As the amount of this material decreases, disks evolve from primordial disks to transitional disks to debris disks. Debris disks, which are found around main-sequence stars, contain little or no primordial material. Instead, they are composed of recently produced secondary material generated by collisions between and evaporation of planetesimals, analogs of solar system asteroids and comets. Terrestrial planet formation may be occurring in the younger debris disks, while the older ones seem to correspond to the "clearing out" stage early in the history of the solar system, during which most leftover planetesimals are removed from the system. Impacts by water-rich planetesimals probably delivered most of the Earth's surface volatiles during the clearing phase (e.g., Morbidelli et al. 2000).

Gas in debris disks is generally hard to detect. Only one bona fide debris disk, 49 Ceti, shows any trace of submillimeter CO emission (Zuckerman et al. 1995; Dent et al. 2005), indicating that debris disk gas abundances are low relative to those in primordial and transitional disks. It appears that primordial molecular gas left over from star formation has largely dissipated by the debris disk phase. However, sensitive UV/optical absorption spectroscopy has revealed small amounts of secondary gas in a few debris disks: β Pictoris (e.g., Lagrange et al. 1998), 51 Ophiuchi (e.g., Roberge et al. 2002), σ Herculis (Chen & Jura 2003), and HD 32297 (Redfield 2007). The gas seen is primarily atomic. The primary production mechanisms for secondary gas in debris disks are currently unknown, but may include photon-stimulated desorption from circumstellar (CS) dust grains (Chen et al. 2007) and/or grain-grain collisions (Czechowski & Mann 2007).

β Pic is the only debris disk whose gas is well characterized. In this disk, most measured gaseous elements have roughly solar abundances relative to each other (Roberge et al. 2006). The exception is carbon, which is extremely overabundant relative to every other measured element (e.g., C/O = 18 $\times$ solar). This discovery was surprising, since the central star has solar metallicity (Holweger et al. 1997). The carbon overabundance suggests that a previously unsuspected—and currently unknown—process is operating in the disk, during which the planetesimals preferentially lose volatile carbonaceous material. However, the lack of similar abundance information for other debris disks renders interpretation of the β Pic results difficult.

Detections of gas in debris disks to date have almost exclusively used optical or UV absorption spectroscopy of edge-on disks. Such observations are sensitive to very small amounts of cold gas. Unfortunately, the geometric constraint that the line of sight to the central star must pass through the disk severely limits the number of disks that may be probed for gas in this way. There is a strong need for additional debris disks in which gas can be observed, in order to study the evolution of gas abundance and composition throughout the entire planet formation phase.

A class of peculiar stars called shell stars may be the avenue toward finding edge-on debris disks containing gas. These are stars whose spectra show narrow absorption lines arising from line-of-sight gas at the velocity of the star. Most shell stars are B or A type. In some cases, the narrow lines may arise from interstellar (IS) material, although the fact that the gas is at the velocity of the star makes this interpretation less likely. In addition, the absorption lines are generally stronger than can be readily explained by IS gas (e.g., Abt & Moyd 1973). The shell stars have high projected rotational velocities compared to nonshell early-type stars, showing that gas is more likely to be detected when the line of sight intersects the rotational plane of the system (e.g., Holweger et al. 1999). This indicates that the gas is usually

[1] NASA Postdoctoral Fellow.

TABLE 1
Target Stars

ID	Other Name	Spectral Type	Distance (pc)	Inside the LIB?	Exposure Times (s)	
					24 μm	70 μm
Main-Sequence Shell Stars from Hauck & Jaschek (2000)						
HD 21620[a]		A0 Vn	143	Yes	37	6965
HD 24863		A4 V	107	Yes	37	3105
HD 39283	ξ Aur	A2 V	74	Yes	37	671
HD 77190[a]	67 Cnc	A8 Vn	59	Yes	37	2685
HD 98353[a]	55 UMa	A2 V	56	Yes	37	420
HD 118232	24 Cvn	A5 V	58	Yes	37	294
HD 142926	4 Her	B9p V	148	Yes	37	2853
HD 158352		A8 V	63	Yes	37	797
HD 196724	29 Vul	A0 V	65	Yes	37	671
HD 199603[a]		A9 V	85	Yes	37	2685
HD 223884		A5 V	92	Yes	37	3483
HD 224463		F2 V	108	Yes	37	4280
Shell Stars with Time-Variable Infalling Gas						
HD 42111[a]		A3 Vn	187	No	37	3609
HD 50241	α Pic	A7 IV	30	Yes	37	168
HD 148283[a]	25 Her	A5 V	79	Yes	37	671
HD 217782[a]	2 And	A3 Vn	107	Yes	37	545

[a] Binary system.

confined to that plane and strengthens the case for a CS rather than IS origin of most shell absorption lines.

Many shell stars appear to be rapidly rotating evolved stars that have recently ejected mass from their equatorial planes. However, Hauck & Jaschek (2000) evaluated the luminosity classes of 57 shell stars and found that 40% of them are main-sequence stars. The nature of the main-sequence shell stars is not fully understood. Some are rapidly rotating classical Be stars with hot excretion disks. We note, however, that 6 out of the 23 main-sequence stars in the Hauck & Jaschek (2000) sample have protoplanetary or debris disks. Among the six are the well-known disk systems β Pic, HD 163296, and MWC 480. In fact, β Pic was classified as a shell star a decade before discovery of its dust disk (Slettebak 1975).

In this paper, we present a study aimed at finding additional debris disks hiding among the shell stars. We used the Multiband Imaging Photometer for *Spitzer* (MIPS) on the *Spitzer Space Telescope* to measure the fluxes from 16 nearby main-sequence shell stars at 24 and 70 μm. The observations were designed to probe sensitively for excess flux arising from CS dust. The goal is to assemble a unique and valuable set of debris disk systems where the gas may be studied in as much detail as the dust.

2. TARGET SELECTION AND OBSERVATIONS

We began our target selection by considering which subset of the 57 shell stars in Hauck & Jaschek (2000) is the most likely to contain debris disks. To eliminate evolved stars, we selected only the stars with luminosity class V (23 stars). We then eliminated six stars already known to have protoplanetary or debris disks. We also wanted to eliminate ordinary stars that might have been misclassified as shell stars simply because they have anomalously large amounts of IS material along their lines of sight. Therefore, we discarded stars that are outside the Local Interstellar Bubble (LIB), using the LIB size and shape from Lallement et al. (2003). This left us with 12 stars (listed in Table 1).

To this set, we added four shell stars whose spectra show narrow, time-variable absorption features. These are HD 42111 (Lecavelier des Etangs et al. 1997), HD 50241 (Hempel & Schmitt 2003), HD 148283 (Grady et al. 1996), and HD 217782 (Cheng & Neff 2003). The time-variability confirms that the gas along the lines of sight to these stars is CS, despite the fact that one of them is outside the LIB. Such behavior is seen in spectra of β Pic and is caused by evaporation of star-grazing planetesimals passing through the line of sight (e.g., Beust et al. 1990). One of the four stars (HD 50241) has luminosity class IV. However, since it has time-variable *infalling* CS gas, it is unlikely to be an evolved mass-losing star.

We obtained MIPS 24 μm images and 70 μm default-scale images for 15 of our 16 target stars. For one of our stars (HD 77190), we obtained only a 70 μm observation. This star was observed at 24 μm in GTO program 40; we used that image in our study. All the data were calibrated with version S13.2.0 of the *Spitzer* Science Center (SSC) calibration pipeline software. The total exposure times for each star are listed in the last two columns of Table 1.

3. ANALYSIS

3.1. 24 μm *Photometry*

To determine the 24 μm fluxes from the target stars, we used the pipeline-processed post–Basic Calibrated Data (BCD) mosaic images, which are suitable for detailed analysis. The pixels in these images are 2.45×2.45. Every target star was detected at S/N $\geq$ 50, except for the faintest (HD 224463), which was detected at S/N = 7. The locations of the star centers were determined by fitting a two-dimensional Gaussian to each star.

For most of the target stars, we performed aperture photometry using an object aperture and sky annulus combination close to the 24 μm large-aperture combination used in Su et al. (2006; $r_{\rm obj} = 14.7''$, $r_{\rm sky\ inner} = 29.4''$, and $r_{\rm sky\ outer} = 41.7''$). The aperture correction for this combination is 1.143. For three of the targets, there are nearby faint stars or background objects that fall within the default object aperture or sky annulus. In these cases,

TABLE 2
PHOTOMETRY APERTURES AND APERTURE CORRECTIONS

Wave (μm)	r_{object} (arcsec)	$r_{sky\ inner}$ (arcsec)	$r_{sky\ outer}$ (arcsec)	Aperture Correction	Comment
24	14.7	29.4	41.7	1.143	Default[a]
24	14.7	39.2	49.0	1.135	Used for HD 42111[b]
24	14.7	19.6	29.4	1.154	Used for HD 158352[b]
24	9.8	19.6	31.9	1.322	Used for HD 199603[b]
70	28.0	40.0	68.0	1.298	Default[a]
70	16.0	40.0	64.0	1.884	Used for HD 39283, HD 77190, HD 42111, and HD 158352[c]
70	8.0	40.0	64.0	4.186	Used for HD 199603[c]

[a] From Su et al. (2006).
[b] Calculated from our data. See § 3.1.
[c] From the SSC Web site (http://ssc.spitzer.caltech.edu/mips/apercorr).

we used aperture and annulus combinations that avoid the nearby sources. Aperture corrections for these combinations were calculated using the 24 μm image of our brightest target star at this wavelength (HD 50241). To verify the accuracy of our calculated corrections, we used that image to calculate a correction for the Su et al. (2006) aperture combination given above. Our calculated correction differed from the published Su et al. (2006) correction by only 0.5%. All the apertures, annuli, and corrections used appear in Table 2.

The results of our aperture photometry, which have not been color corrected, appear in Table 3. The uncertainties in the flux measurements were determined in the following way. The aperture photometry equation giving the fluxes in mJy is

$$F = cAp\left(\sum_{i,j} f_{i,j} - N\overline{s}\right), \quad (1)$$

where c is a units conversion factor (0.023504 mJy sr arcsec^{-2} MJy^{-1}), A is the aperture correction, p is the angular size of the pixels (2.45^2 arcsec^2), $f_{i,j}$ is the surface brightness value of pixel i, j in units of MJy sr^{-1}, N is the number of pixels in the object aperture, and $\overline{s}$ is the mean sky brightness calculated from the pixels in the sky annulus. The sum is taken over all the pixels in the object aperture. This equation may be reduced to

$$F = C\left(\sum_{i,j} f_{i,j} - B\right), \quad (2)$$

where C is a constant and B is the estimate of the background flux in the object aperture. Propagating uncertainties gives the following equation for the uncertainty in the total flux:

$$\sigma_F = C\sqrt{\sum_{i,j} \sigma_{s_{i,j}}^2 + \sigma_B^2}, \quad (3)$$

where the $\sigma_{s_{i,j}}$ are the uncertainties in the surface brightness values and σ_B is the uncertainty in the estimate of the background flux in the object aperture.

The $\sigma_{s_{i,j}}$ values were taken from the uncertainty array provided by the SSC calibration pipeline. To estimate σ_B, we placed eight apertures and sky annuli in empty regions around each star. For each empty aperture, the difference between the actual value of B and the value estimated from the pixels in the sky annulus was calculated. The standard deviation of the differences was taken

TABLE 3
PHOTOMETRY RESULTS

	24 μm					70 μm				
ID	$F_\star$ (mJy)	F_{MIPS} (mJy)	σ_{MIPS} (mJy)	$[(F_{MIPS} - F_\star)/F_\star]100$ (%)	Excess?	$F_\star$ (mJy)	F_{MIPS} (mJy)	σ_{MIPS} (mJy)	$[(F_{MIPS} - F_\star)/F_\star]100$ (%)	Excess?
HD 21620	27.31	34.11	0.64	24.88 ± 2.34	Yes	3.3	24.2	6.5	640.1 ± 199.1	Yes
HD 24863	25.06	28.01	0.55	11.77 ± 2.20	No	3.0	<19.4	5.3	<545.4	No
HD 39283	84.22	84.88	0.70	0.79 ± 0.83	No	10.1	<23.5	5.7	<133.9	No
HD 77190	45.08	48.81	0.50	8.29 ± 1.12	No	5.4	<16.2	3.5	<200.1	No
HD 98353	108.95	114.52	0.53	5.11 ± 0.49	No	13.0	<54.1	12.3	<315.3	No
HD 118232	111.10	155.67	0.49	40.12 ± 0.44	Yes	13.3	81.4	7.6	513.7 ± 57.2	Yes
HD 142926	28.55	107.52	0.51	276.66 ± 1.79	Yes	3.4	25.4	6.3	651.6 ± 186.8	Yes
HD 158352	74.02	103.44	0.35	39.75 ± 0.47	Yes	8.9	235.1	7.3	2551.2 ± 82.8	Yes
HD 196724	73.44	75.21	0.46	2.41 ± 0.63	No	8.7	17.2	4.9	97.0 ± 56.2	No
HD 199603	44.71	50.54	0.38	13.04 ± 0.85	No	5.4	18.2	3.8	239.7 ± 71.0	Yes[a]
HD 223884	34.45	37.23	0.39	8.06 ± 1.13	No	4.1	<21.1	4.5	<412.2	No
HD 224463	3.79	4.07	0.59	7.50 ± 15.51	No	0.5	<11.7	3.6	<2469.1	No
HD 42111	47.02	51.13	0.74	8.73 ± 1.56	No	5.6	<9.0	3.0	<59.7	No
HD 50241	608.29	647.56	0.42	6.46 ± 0.07	No	73.0	75.9	9.7	4.0 ± 13.3	No
HD 148283	66.95	71.03	0.43	6.10 ± 0.64	No	8.0	<21.2	5.2	<164.4	No
HD 217782	88.28	92.10	0.56	4.33 ± 0.63	No	10.6	<41.9	10.4	<296.8	No

[a] This "excess" is probably caused by a nearby source.

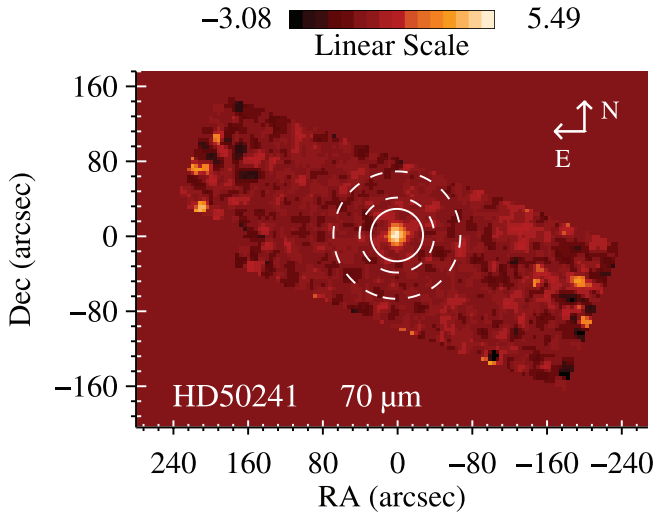

FIG. 1.—MIPS 70 μm image of HD 50241. The mosaic was created using MOPEX. The pixels are 4.0 × 4.0. The default object aperture used for the 70 μm photometry is overlaid with a solid white line. The default sky annulus is shown with dashed white lines.

as the estimate of σ_B. This method of calculating the flux uncertainties includes object noise, noise due to variations of the background within the sky annulus, and noise due to spatial variations of the background between the object aperture and the sky annulus.

We calculated the median background surface brightness in each image using pixels between 61″ and 135″ from the target star. The background values range from 17.3 MJy sr^{-1} (low) to 49.7 MJy sr^{-1} (medium high). The definitions of low, medium, and high background levels may be found on the SSC Web site.[2] For our target stars, variation of the background between the object aperture and the sky annulus appears to be responsible for 18% to 67% of the total flux uncertainty.

3.2. 70 μm *Photometry*

Since the 70 μm post-BCD mosaic images are not suitable for detailed analysis, we used the SSC software MOPEX to combine the filtered BCD images. MOPEX was set to propagate the uncertainty images from the SSC pipeline and to use multiframe temporal outlier rejection, since all the mosaics have good coverage values (>10 exposures in the regions around the target stars). The pixels in the final mosaics are 4.0 × 4.0. One of the final 70 μm mosaics is shown in Figure 1. Seven of the 16 target stars were detected at 70 μm with S/N ≥ 3. Since many of the stars were not detected, we used the telescope pointing information in the image headers to determine the locations of the star centers.

For most of the stars, we used an object aperture and sky annulus combination close to the 70 μm large-aperture combination used in Su et al. (2006; $r_{\rm obj} = 28.0''$, $r_{\rm sky\ inner} = 40.0''$, and $r_{\rm sky\ outer} = 68.0''$). The default object aperture and sky annulus are overlaid on the 70 μm mosaic shown in Figure 1. For stars with nearby faint sources in the 24 μm images, we used aperture and annulus combinations that avoided the sources, even if they were not visible in the 70 μm images. The aperture corrections for these combinations were taken from tables available on the SSC Web site.[3] All the apertures, annuli, and corrections used appear in Table 2. The 70 μm photometry results, which have not been color corrected, appear in Table 3.

We calculated the uncertainties in the 70 μm fluxes following the same procedure used for the 24 μm photometry (described in § 3.1). For each star not detected at the 3 σ level, a conservative upper limit on the 70 μm flux was set by adding 3 times the total statistical uncertainty to any positive flux measured in the object aperture. The median background surface brightnesses near the target stars were estimated from the unfiltered post-BCD mosaic images, using pixels between 48″ and 80″ from the stars. The background values range from 5.8 MJy sr^{-1} (low) to 16.3 MJy sr^{-1} (medium). At 70 μm, background variation between the object aperture and the sky annulus appears to be responsible for 43% to 84% of the total flux uncertainty for our target stars.

4. SPECTRAL ENERGY DISTRIBUTIONS

4.1. *Fitting Photospheric Models*

To see whether any of the target stars show excess IR emission, we first needed to determine their expected photospheric fluxes at 24 and 70 μm for comparison to the observed fluxes. This was done by fitting stellar models to the optical and near-IR fluxes from the stars. *B* and *V* magnitudes from the Tycho-2 Catalogue (Høg et al. 2000) were converted to Johnson magnitudes using formulae given in Volume 1 of the *Hipparcos* and Tycho catalogs,[4] then to flux densities. The near-IR magnitudes in the *J*, *H*, and K_s bands from the 2MASS Catalog were converted to flux densities using the zero points given in the 2MASS Explanatory Supplement.[5]

Since all but one of the target stars are within the LIB, we did not apply an IS extinction correction to the optical and near-IR photometry. Kurucz model photospheric spectra, with $\log g = 4.0$ for the stars with spectral types earlier than A5 and $\log g = 4.5$ for the cooler stars, were fit to the optical and near-IR fluxes using χ^2 minimization. The best-fitting model spectrum for each star was used to calculate the predicted photospheric fluxes at 24 and 70 μm, which appear in Table 3.

We then considered whether any of the stars showed significant excess flux at either wavelength. The excesses were characterized by calculating the percent deviation of the measured flux from the predicted photospheric flux, while propagating the statistical uncertainties in the measured fluxes (see Table 3). First, we compared the excesses to the uncertainties in the absolute photometric calibration of MIPS data processed with version S13 of the SSC calibration pipeline. The uncertainties are 4% for 24 μm data and 7% for 70 μm data (MIPS Data Handbook, ver. 3.2). We conservatively designated excesses greater than 5 times these uncertainties as significant, which corresponds to >20% at 24 μm and >35% at 70 μm. The second criterion for a significant excess is that it must be at least 3 times greater than its propagated statistical uncertainty. This criterion eliminated apparent excesses only at 70 μm.

Four of the 16 stars showed significant 24 μm excesses (HD 21620, HD 118232, HD 142926, and HD 158352). These stars also showed significant 70 μm excesses. The spectral energy distributions (SEDs) of all the target stars are shown in Figure 2. One additional star, HD 199603, showed a significant 70 μm excess. However, the source visible in the 70 μm image of HD 199603 is slightly offset from the expected position of the A star; it is located at the position of a nearby faint source visible in the 24 μm image of HD 199603. Therefore, we believe that the apparent 70 μm excess from HD 199603 is due to contamination from this nearby red source, despite our care in aperture selection. The nature of this nearby red source is not yet known.

[2] See http://ssc.spitzer.caltech.edu/obs/bg.html.
[3] See http://ssc.spitzer.caltech.edu/mips/apercorr.
[4] See http://www.rssd.esa.int/Hipparcos/CATALOGUE_VOL1/sect1_03.pdf.
[5] See http://www.ipac.caltech.edu/2mass/releases/allsky/doc/sec6_4a.html.

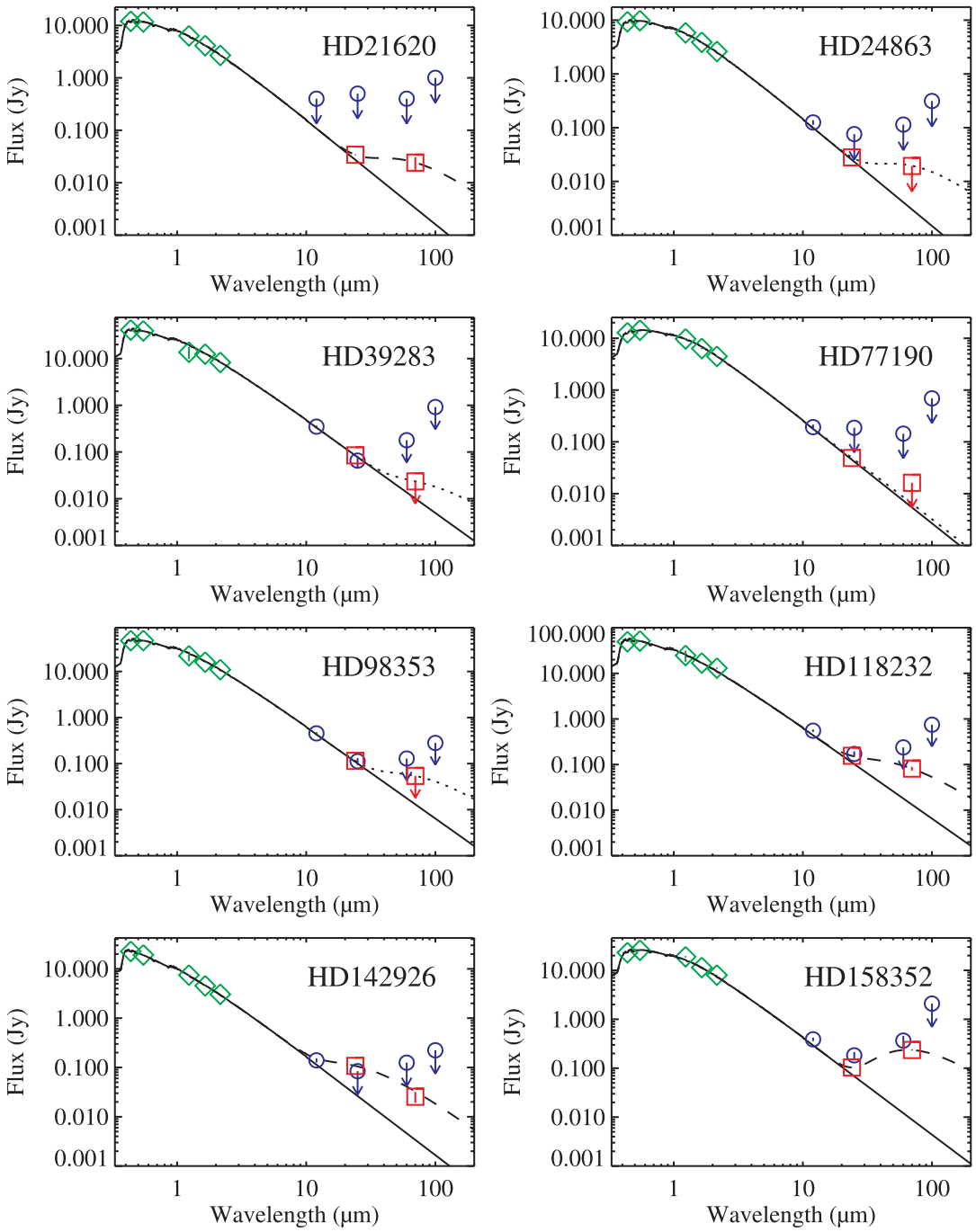

FIG. 2.—SEDs of the target stars. The fluxes in the *B* and *V* bands from the Tycho-2 Catalogue and the *J*, *H*, and K_s bands from the 2MASS Catalog are plotted with green diamonds. Color-corrected fluxes from *IRAS* are plotted with blue circles. The new 24 and 70 μm MIPS fluxes, which have not been color corrected, are plotted with red squares. Upper limits are indicated with arrows. Uncertainties in the flux measurements are overplotted with straight vertical lines. The best-fitting Kurucz model photospheric spectra are overplotted with solid black lines. In each panel, the total SED model (the sum of the stellar model and a single-temperature blackbody model) is shown with dashed or dotted black lines. The blackbody temperatures and L_{IR}/L_* values for these models are given in Table 4. For the four stars with significant IR excess emission at the MIPS wavelengths (HD 21620, HD 118232, HD 142926, and HD 158352), the best-fitting total SED model is shown with a dashed line. For the stars without significant IR excesses, the total SED model showing the upper limit on the IR excess emission is overplotted with a dotted line.

For the rest of the target stars, the mean 24 μm excess is 6.3% $\pm$ 3.1%. There is a small positive offset, although it is not significant at the 3 σ level. Ordinarily, this would indicate a problem with the photospheric modeling or with the aperture photometry itself. However, we do not believe this to be case. The photometry should be accurate, since the MIPS color corrections for early-type stars are extremely small. The photospheric modeling appears accurate. The average deviation between the fitted effective temperatures and the expected effective temperatures (based on the spectral types) is only 378 K. The accuracy of the fitted effective temperatures also indicates that IS reddening does not significantly affect the photospheric model fitting.

The small positive offset measured at 24 μm may be real. None of the target stars are unambiguously nonexcess stars, since they are all main-sequence shell stars with CS gas. If they are not debris disks or protoplanetary disks, then they may be classical Be stars, which show small, hot mid-IR excesses from free-free emission (see Fig. 6 in Su et al. 2006). We plan additional studies to